

Neural Additive Image Model: Interpretation through Interpolation

Arik Reuter

*Data Science Working Group
Institute of Mathematics
Clausthal University of Technology
8678 Clausthal-Zellerfeld, Germany*

ARIK.REUTER@CAMPUS.LMU.DE

Anton Thielmann

*Data Science Working Group
Institute of Mathematics
Clausthal University of Technology
8678 Clausthal-Zellerfeld, Germany*

ANTON.THIELMANN@TU-CLAUSTHAL.DE

Benjamin Saefken

*Data Science Working Group
Institute of Mathematics
Clausthal University of Technology
8678 Clausthal-Zellerfeld, Germany*

BENJAMIN.SAEFKEN@TU-CLAUSTHAL.DE

Abstract

Understanding how images influence the world, interpreting which effects their semantics have on various quantities and exploring the reasons behind changes in image-based predictions are highly difficult yet extremely interesting problems. By adopting a holistic modeling approach utilizing Neural Additive Models in combination with Diffusion Autoencoders, we can effectively identify the latent hidden semantics of image effects and achieve full intelligibility of additional tabular effects. Our approach offers a high degree of flexibility, empowering us to comprehensively explore the impact of various image characteristics. We demonstrate that the proposed method can precisely identify complex image effects in an ablation study. To further showcase the practical applicability of our proposed model, we conduct a case study in which we investigate how the distinctive features and attributes captured within host images exert influence on the pricing of Airbnb rentals.

Keywords: Interpretable Deep Learning, Neural Additive Models, Diffusion Autoencoders, Image Interpretation, Global Interpretability

1 Introduction

Over the last decade, Deep Neural Networks (DNN) have achieved remarkable results in a variety of tasks. Text classification (Kowsari et al., 2019), Speech Recognition (e.g. (Radford et al., 2022; Ma et al., 2022)), Computer Vision (O’Mahony et al., 2020), Genome Detection (Danaee et al., 2017) or Protein Folding (Jumper et al., 2021) are just a few areas in which DNNs have considerably exceeded their predecessors, sometimes by astonishingly wide margins. The flexibility and predictive power of DNNs, however, often comes at the price of inherently uninterpretable model predictions, leading to DNNs not being used in high risk domains.

Achieving a comprehensive understanding of the inner workings and decision-making processes of these complex models has significant implications for their practical deployment. Various techniques have been proposed to enhance the interpretability of neural networks, including post-hoc methods, as well as a-priori approaches. To differentiate between different forms of model interpretability, we follow the literature (e.g. (Zhang et al., 2021; Fan et al., 2021)) and distinguish between Local and Global interpretability as well as Post-hoc and A-priori interpretability. Local Interpretable Model-Agnostic Explanations (LIME) (Ribeiro et al., 2016), Shapley values (Shapley, 1953) or Layer-wise Relevance Propagation (LRP) (Bach et al., 2015) for example, are post-hoc and locally interpretable methods that are especially well-suited for identifying relevant pixel areas in computer vision related tasks. A-priori and global explanations of model predictions are less commonly adapted and often come with certain disadvantages (Zhang et al., 2021). For instance, Zhang et al. (2018) introduced an a-priori interpretable Convolutional Neural Network (CNN), which is only applicable to classification tasks. For tabular data, Neural Additive Models (NAMs) (Agarwal et al., 2021) are a-priori globally interpretable models that are closely related to Generalized Additive Models (GAMs) (Hastie, 2017; Wood, 2017). NAMs allow to visualize individual feature effects and can incorporate higher order feature interactions. For example, Xu and Guo (2023) in survival analysis and Jo and Kim (2022) in time-series prediction have demonstrated the practical and theoretical relevance of NAMs. Rügamer et al. (2022) extend NAMs to multi-modal data and incorporate images into their modeling framework. However, the unstructured components still lack interpretability, leaving them difficult to comprehend. Therefore, while there exist various model structures that can provide a-priori global interpretability, they are confined to a specific singular data type.

In the domain of computer vision, the recent advancements in generative modelling based on diffusion models allow to produce highly realistic and detailed images across a wide range of styles and subjects (Sohl-Dickstein et al., 2015; Ho et al., 2020). These models operate by gradually constructing an image through a process that starts with random noise and progressively refines it into a coherent output, simulating the reverse of a diffusion process. This approach has demonstrated remarkable capabilities in generating images that are not only visually compelling but also exhibit a high degree of diversity and control over the generation process (Dhariwal and Nichol, 2021; Nichol et al., 2021). Applications of diffusion models extend beyond image synthesis to tasks such as image-to-image translation, super-resolution, and inpainting, showcasing their versatility and potential to push the boundaries of what is achievable in generative visual content creation (Saharia et al., 2022; Yue et al., 2024; Lugmayr et al., 2022).

By utilizing Diffusion Autoencoders (DAEs), a variant Diffusion Probabilistic Models that allows to encode and decode images into a semantically meaningful embedding space (Preechakul et al., 2022), we are able to comprehensively interpret image effects in an additive modelling framework, that incorporates numerical, as well as image-covariates.

Multi-modal data, comprising tabular data as well as images, is not only common in everyday life, but also prevalent in high-risk domains, such as human-resource-management and healthcare. For instance, combining images and, e.g., patient information in tabular form can facilitate a more comprehensive understanding of medical decision-making processes. In summary, this paper aims to make the following contributions:

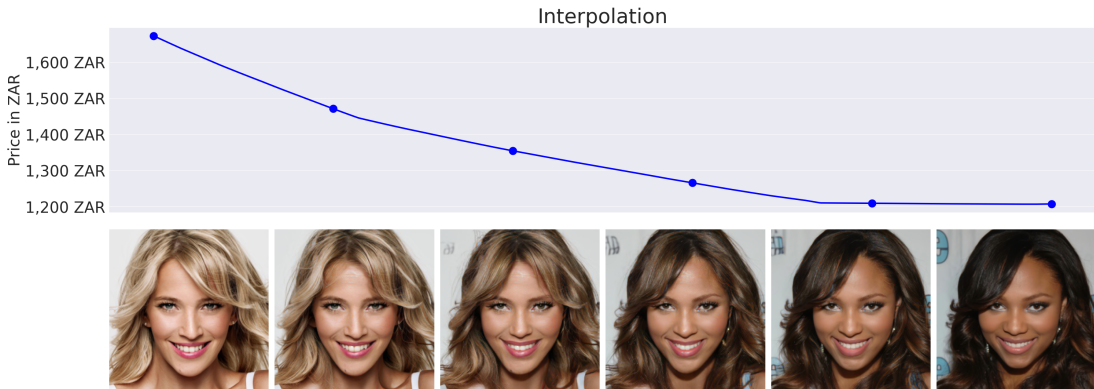


Figure 1: Effect on the price of an Airbnb listing obtained by interpolating between two input images. A Neural Additive Model that includes an image effect is used to predict the expected price. Image Interpolating is achieved by linearly interpolating between image representations in the embedding space of a Diffusion Autoencoder.

- We present a model structure that seamlessly incorporates tabular data and images while preserving global interpretability through the utilization of additivity constraints.
- Our framework for understanding tabular data and images is highly intuitive, flexible, and provides profound insights into the data.
- We experimentally validate the effectiveness of the NAIM framework in identifying the effects of numerical features combined with image-covariates in an ablation study with synthetic data.
- We showcase the effectiveness of the approach and present both global feature effects and locally interpretable examples in a case study.

2 Neural Additive Image Model

Let $\mathcal{D} = \{(\mathbf{x}^{(i)}, y^{(i)})\}_{i=1}^n$ be a dataset of size n . Let further $y \in \mathbb{R}$ denote the target variable that can be arbitrarily distributed and J denote the number of features such that each input $\mathbf{x} = (x_1, x_2, \dots, x_J) \in \mathbb{R}^J$ contains J features. Given a link function $g : \mathbb{R} \rightarrow \mathbb{R}$, a GAM in its most fundamental form can be expressed as:

$$g(\mathbb{E}[y|\mathbf{x}]) = \beta_0 + \sum_j^J f_j(x_j), \tag{1}$$

where β_0 denotes the global intercept and $f_j : \mathbb{R} \rightarrow \mathbb{R}$ denote the univariate shape functions corresponding to input feature x_j . In classical GAMs $f_j \in \mathcal{C}^2(\mathbb{R})$, i.e. the shape functions are smooth, two times differentiable functions, e.g., cubic splines and the parameters are optimized via a penalized least squares criterion (Hastie, 2017; Wood, 2017). The effects of features on the target variable are finally interpreted by, e.g., plotting the graph of the shape

function. Pairwise feature interactions are often accounted for in the form of:

$$g(\mathbb{E}[y|\mathbf{x}]) = \beta_0 + \sum_j^J f_j(x_j) + \sum_{j,k:j \neq k}^J f_{jk}(x_j, x_k), \quad (2)$$

where $f_{jk} : \mathbb{R}^2 \rightarrow \mathbb{R}$ denote all feature interactions between input features $(x_j, x_k) \in \mathbb{R}^2$.

Nori et al. (2019) introduced tree-based, cyclic gradient boosting GAMs, resulting in much more powerful, yet interpretable GAMs. Similarly, Chang et al. (2021) used differentiable decision trees. Dubey et al. (2022) introduced scalable polynomials as shape functions.

Neural Additive Models (NAMs) on the other hand leverage multilayer perceptrons (MLPs) as shape functions while preserving the overall additive model structure (Agarwal et al., 2021). This enables the development of interpretable and powerful models that leverage the advantages inherent to the deep learning paradigm. Thus, higher order feature interactions can be accounted for in various ways, by, e.g. adding higher-dimensional input MLPs directly into Equation 2 (Enouen and Liu, 2022; Kim et al., 2022). Through the inherent flexibility of MLPs, further adaptations, e.g. shared learned basis functions (Radenovic et al., 2022; Enouen and Liu, 2022) or distributional approaches (Thielmann et al., 2023) are possible.

Additionally, independent of the shape function, fitting the model with gradient descent allows for other data types to be incorporated into the modelling, that traditional GAMs are not able to account for. While all GAM adaptations achieve remarkable results in terms of predictive performance, only Rügamer et al. (2022) incorporated images into their GAM. However, the unstructured parts remain completely uninterpretable.

To account for interpretable image effects, we adapt Equation 2 accordingly. Let further \mathbf{x} denote the tabular features, where x_j is the j -th tabular feature, and \mathbf{x}_{img} denotes the images. Equation 2 can subsequently be adapted to:

$$g(\mathbb{E}[y|\mathbf{x}, \mathbf{x}_{img}]) = \beta_0 + \sum_j^J f_j(x_j) + \sum_{j,k:j \neq k}^J f_{jk}(x_j, x_k) + f_{img}(\mathbf{E}_\phi(\mathbf{x}_{img})), \quad (3)$$

where \mathbf{E}_ϕ denotes a CNN with parameters ϕ that encodes an input image into a latent representation $\mathbf{z} = \mathbf{E}_\phi(\mathbf{x}_{img}) \in \mathbb{R}^l$. This latent representation is subsequently processed by the image-specific shape function $f_{img} : \mathbb{R}^l \rightarrow \mathbb{R}$. Note that Equation 3 can be directly adapted to include interactions between numerical and image covariates.

2.1 Interpretable Image Representations

Diffusion Autoencoders (DAEs) (Preechakul et al., 2022) are a powerful class of autoencoders that can provide semantically meaningful and almost perfectly decodable latent representations of images. The key innovation of DAEs is the use of a semantic encoder in combination with a Denoising Diffusion Implicit Model (DDIM) (Song et al., 2020). The semantic encoder captures high-level features of an input image while the DDIM acts as both an encoder of more subtle stochastic variations in the input image and as a powerful decoder. More specifically, the semantic encoder \mathbf{E}_ϕ provides a semantic subcode $\mathbf{z} = \mathbf{E}_\phi(\mathbf{x}_{img})$ that encodes primarily the high-level information for a given input image \mathbf{x}_{img} . The DDIM, on the other hand, can map a stochastic subcode $\mathbf{x}_{img}^{(T)}$, for instance, sampled from a standard-normal distribution, onto a real-world image.

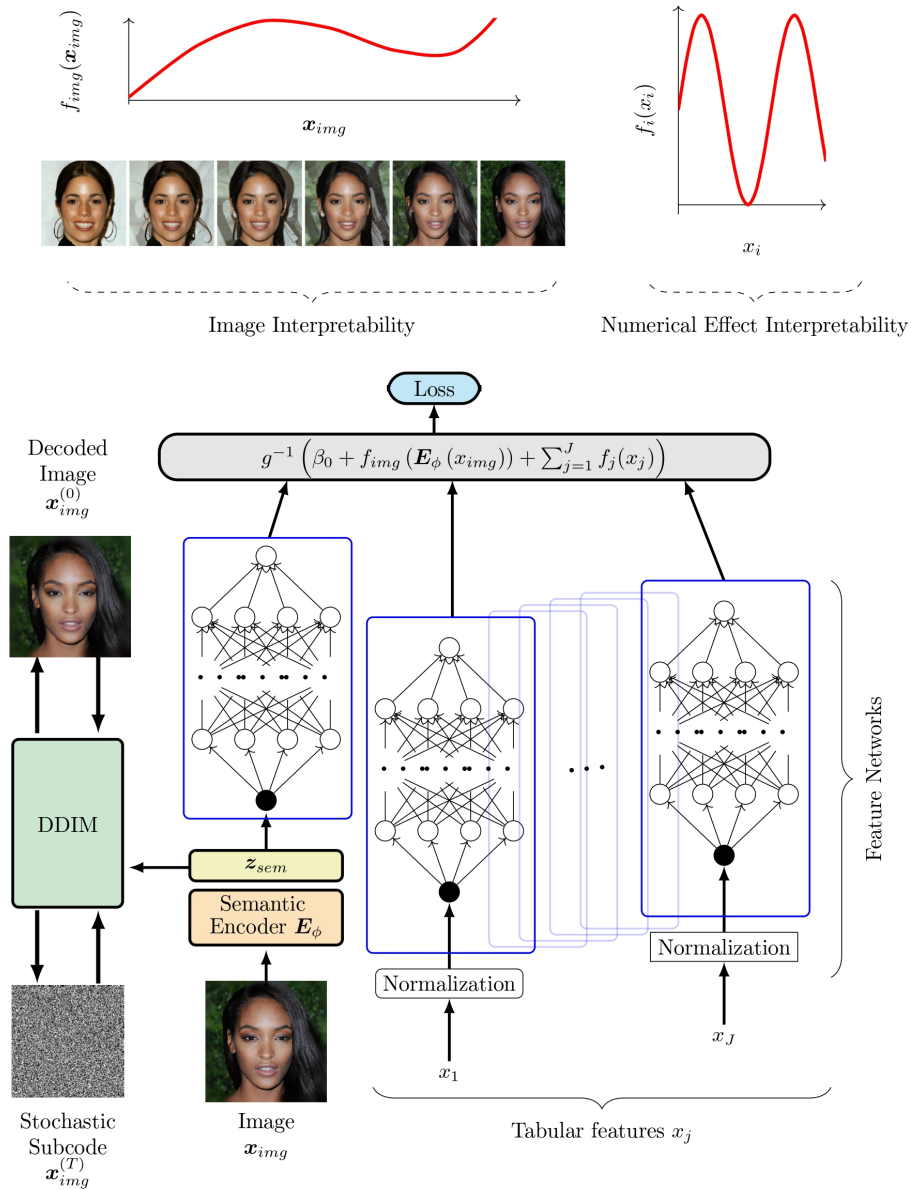


Figure 2: Model architecture of the base version of the proposed approach not accounting for interaction effects. The tabular data is fit as independent MLPs, the images are encoded with an CNN encoder and fit with a separate MLP. All feature effects are summed up for the model prediction.

This is achieved by denoising the noise-input in a step-wise manner until the final image is generated. The reverse diffusion process that is used to generate the image from the

stochastic subcode can be described as follows:

$$p_\psi(\mathbf{x}_{img}^{(0:T)}|\mathbf{z}) = p(\mathbf{x}_{img}^{(T)}) \prod_{t=1}^T p_\psi(\mathbf{x}_{img}^{(t-1)}|\mathbf{x}_{img}^{(t)}, \mathbf{z}), \quad (4)$$

where ψ denotes the parameters of the DDIM and the semantic subcode \mathbf{z} is used to condition the image generation on the high-level semantics of the reconstructed image. Further, $p_\psi(\mathbf{x}_{img}^{(t-1)}|\mathbf{x}_{img}^{(t)}, \mathbf{z})$ is given by:

$$p_\psi(\mathbf{x}_{img}^{(t-1)}|\mathbf{x}_{img}^{(t)}, \mathbf{z}) = \begin{cases} \mathcal{N}(f_\psi(\mathbf{x}^{(1)}, 1, \mathbf{z}), 0) & \text{if } t = 1 \\ q(\mathbf{x}_{img}^{(t-1)}|\mathbf{x}_{img}^{(t)}, f_\psi(\mathbf{x}_{img}^{(t)}, t, \mathbf{z})) & \text{otherwise.} \end{cases}$$

f_ψ is parameterized as a noise prediction network as done in Preechakul et al. (2022) and $q(\mathbf{x}_{img}^{(t-1)}|\mathbf{x}_{img}^{(t)}, \mathbf{x}_{img}^{(0)})$ defines the inference distribution matched by the reverse generative process (4).

Since DDIMs have a deterministic generative process, they can be interpreted as autoencoders, which can not only decode the stochastic code \mathbf{x}_T into an image, but also encode an image into a corresponding stochastic (sub-)code by running the generative process backwards. For diffusion autoencoders, the encoding procedure is enhanced by also conditioning on \mathbf{z} , which does not only improve image generation by providing the compact semantic information in \mathbf{z} , but thereby also increases inference speed.

The embedding space of the semantic subcode has several advantageous properties: First, every semantic subcode can be decoded and thus visualized. Second, simple linear interpolation between semantic subcodes corresponds to meaningful semantic interpolation in the space of real images. Third, one can obtain interpretations of some directions in the embedding space. Those directions can be, for instance, given by the normal vector of the separating hyperplane corresponding to a linear classifier trained on the semantic codes.

2.2 Image-Effect Interpretation through Interpolation

NAMs provide a framework to globally interpret the effects of continuous features by plotting the graph of the shape functions f_j corresponding to the respective univariate (or sometimes bivariate) covariates. However, since image-data lacks any inherently semantically interpretable dimensions in pixel-space, one has to rely on meaningful image representations, their semantics and interpretations, in order to achieve similar understanding of image data. An important, and often existing property, of those learned representations is **semantic continuity**, i.e. representations that are close in their embedding space are also similar in terms of their semantics, as understood by humans (Oh Song et al., 2016; Vinyals et al., 2016; Bell and Bala, 2015). One can formalize this by assuming a bijective function $m : \mathbb{R}^p \rightarrow \mathbb{R}^l$ that maps a ground-truth semantic feature $\Phi(\mathbf{x}_{img})$ of an image \mathbf{x}_{img} onto the embedding $\mathbf{E}_\phi(\mathbf{x}_{img})$ of that image, i.e. $m = \mathbf{E}_\phi \circ \Phi^{-1}$ if Φ is invertible. Examples for those ground-truth features obtained by Φ could be the average red-value of all pixels in an RGB-image, the age of a portrayed person or the position of an object. We can now define semantic continuity as assuming regularity, i.e., continuity in the mathematical sense, or more general different degrees of smoothness for m .

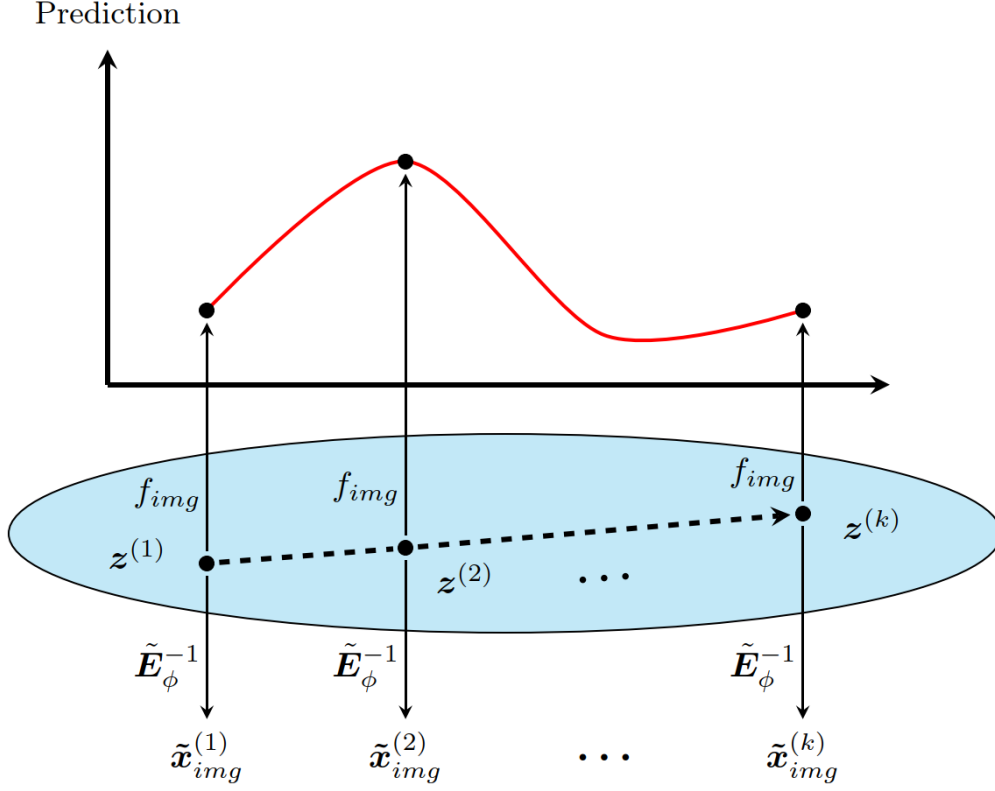


Figure 3: Interpolating between the latent semantic codes $\mathbf{z}_{int}^{(1)}$ and $\mathbf{z}_{int}^{(k)}$ in the embedding space can be visualize in pixel-space as the sequence $(\tilde{\mathbf{x}}_{img}^{(1)}, \tilde{\mathbf{x}}_{img}^{(2)}, \dots, \tilde{\mathbf{x}}_{img}^{(k)})$ by using the decoder $\tilde{\mathbf{E}}_{\phi}^{-1}$ on the latent codes. Each latent code \mathbf{z}_{int} , on the other hand, also allows to make the prediction $f_{img}(\mathbf{z}_{int})$ for a response variable of interest. Plotting the predictions $(f_{img}(\mathbf{z}_{int}^{(1)}), f_{img}(\mathbf{z}_{int}^{(2)}), \dots, f_{img}(\mathbf{z}_{int}^{(k)}))$ against the generated images $(\tilde{\mathbf{x}}_{img}^{(1)}, \tilde{\mathbf{x}}_{img}^{(2)}, \dots, \tilde{\mathbf{x}}_{img}^{(k)})$ allows to investigate the image effect.

To obtain human insight into the mostly incomprehensible nature of representations obtained by deep learning methods, a straightforward requirement is **decodability**. This property of embeddings implies that there is not only a way to encode an image into a semantic representation, via $\mathbf{z} = \mathbf{E}_{\phi}(\mathbf{x}_{img})$ but also always the possibility to translate any latent code back to the pixel level, i.e. an image which can be intuitively understood by humans. This can be interpreted as being able to approximate the inverse of the encoding function \mathbf{E}_{ϕ} via $\tilde{\mathbf{E}}_{\phi}^{-1} \approx \mathbf{E}_{\phi}^{-1}$. One can note that in the context of DAEs (Preechakul et al., 2022), embeddings do not only posses great properties in terms of semantic continuity, but are seminal in terms of near-perfect decodability.

For the purpose of image-effect interpretation, semantic continuity allows to locally change embeddings in a semantically meaningful way, while the decodability ensures that those changes can be visualized. A sequence of latent representation $(\mathbf{z}^{(i)})_{i=1}^k := (\mathbf{z}^{(1)}, \mathbf{z}^{(2)}, \dots, \mathbf{z}^{(k)})$

then corresponds to a series of generated images. If the augmented latent representations are also used to make predictions, one can visualize the effect of changing the embeddings by plotting the prediction against the augmented images. In the NAIM framework, this means that we can plot the effect $f_{img}(\mathbf{z}^{(i)})$ against images $\tilde{\mathbf{E}}_\phi^{-1}(\mathbf{z}^{(i)})$ for a selection of k shifted embeddings $(\mathbf{z}^{(i)})_{i=1}^k$. More precisely, the idea is to plot tuples of images, based on decoded embeddings, and corresponding predictions $(\tilde{\mathbf{E}}_\phi^{-1}(\mathbf{z}^{(i)}), f_{img}(\mathbf{z}^{(i)}))_{i=1}^k$ based on a sequence $(\mathbf{z}^{(i)})_{i=1}^k$. Thus, we can visualize a (semi-)continuous feature effect of image semantics provided a sequence of latent variables.

The following result shows that interpolation, and in particular linear interpolation, is a reasonable approach for obtaining such a sequence of latent representations $(\mathbf{z}^{(i)})_{i=1}^k$.

Theorem 1 For $h : \mathbb{R}^l \rightarrow \mathbb{R}^p$ a differentiable function one has that

$$h(\lambda \mathbf{z} + (1 - \lambda)\tilde{\mathbf{z}}) = \lambda h(\mathbf{z}) + (1 - \lambda)h(\tilde{\mathbf{z}}) + (1 - \lambda)R \quad (5)$$

for any $\mathbf{z}, \tilde{\mathbf{z}} \in \mathbb{R}^l$ with $0 \leq \lambda \leq 1$ and $R = \mathbf{o}(\|\mathbf{z} - \tilde{\mathbf{z}}\|)$. A proof for this theorem can be found in appendix A.1. Note that the approximation becomes (locally) exact if h is (locally) affine. This theorem demonstrates that first forming the convex combination between two sufficiently close embeddings $\mathbf{z} = \mathbf{E}_\phi(\mathbf{x}_{img})$ and $\tilde{\mathbf{z}} = \mathbf{E}_\phi(\tilde{\mathbf{x}}_{img})$ followed by computing ground-truth semantic features $\Phi(\mathbf{x}_{img}) = m^{-1}(\mathbf{z})$ and $\Phi(\tilde{\mathbf{x}}_{img}) = m^{-1}(\tilde{\mathbf{z}})$ is approximately equal to first computing the semantic features and then forming the convex combination between the semantic features $m^{-1}(\mathbf{z})$ and $m^{-1}(\tilde{\mathbf{z}})$. (Note that $m^{-1} = \Phi \circ \mathbf{E}_\phi^{-1}$). More specifically for the NAIM framework, if one has learned an invertible and smooth function \mathbf{E}_ϕ , that respects semantic features in \mathbb{R}^p well, we can expect that interpolating between two sufficiently close embeddings \mathbf{z} and $\tilde{\mathbf{z}}$ followed by decoding with $\tilde{\mathbf{E}}_\phi^{-1}$ yields the same kind of interpolation for the ground-truth semantic features:

$$\Phi(\tilde{\mathbf{E}}_\phi^{-1}((\lambda \mathbf{z} + (1 - \lambda)\tilde{\mathbf{z}}))) \approx \lambda \Phi(\tilde{\mathbf{E}}_\phi^{-1}(\mathbf{z})) + (1 - \lambda)\Phi(\tilde{\mathbf{E}}_\phi^{-1}(\tilde{\mathbf{z}})). \quad (6)$$

We propose two ways of augmenting images for the purpose of obtaining latent sequences $(\mathbf{z}^{(i)})_{i=1}^k$ with the ultimate goal of image effect interpretation: First, to use image interpolation to locally understand how changes in the image influence the prediction for the response variable. This has the benefit that the effect of arbitrary attributes can be analyzed by selecting pairs of examples where one image has a certain attribute and the other does not. In the context of DAEs, this can be achieved by selecting two images, \mathbf{x}_{img} and \mathbf{x}'_{img} , computing $\mathbf{z} = \mathbf{E}_\phi(\mathbf{x}_{img})$ and $\mathbf{z}' = \mathbf{E}_\phi(\mathbf{x}'_{img})$ followed by obtaining the latent sequence $(\mathbf{z}^{(i)})_{i=1}^k$ as a result of simple linear interpolation between the embeddings \mathbf{z} and \mathbf{z}' . This means that

$$(\mathbf{z}^{(i)})_{i=1}^k = \left(\left(1 - \frac{i-1}{k-1} \right) \mathbf{z} + \frac{i-1}{k-1} \mathbf{z}' \right)_{i=1}^k \quad (7)$$

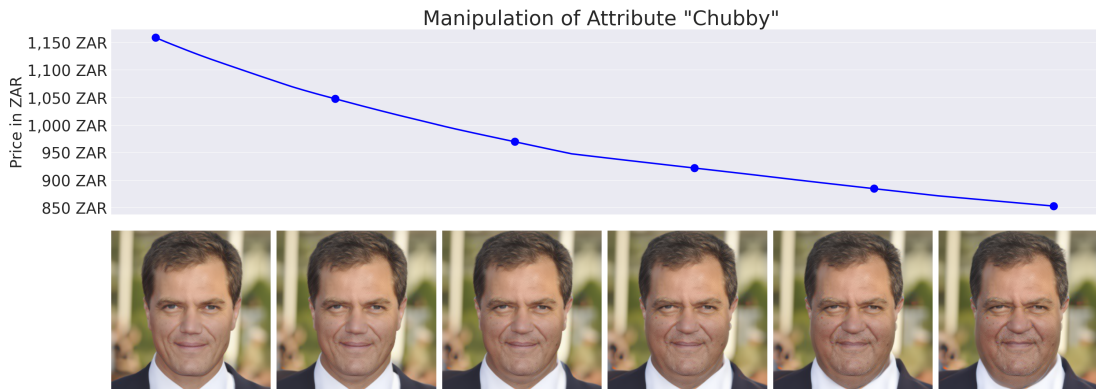


Figure 4: Effect of attribute Manipulation for the feature *Chubby* on the expected rental price. Through (semi) continuous interpolation, an effect trend can be visualized.

Second, attribute manipulation, i.e. the explicit change of a specific semantic quality of an image, can be used to investigate the effect of pre-defined attributes. By explicitly changing an attribute of an image, one can plot the local effect of this change, see, e.g., Figure 4. One can also visualize the global effect that manipulating all training samples has on the distribution of the predictions. Image manipulation can be achieved by shifting the embedding of an input image $\mathbf{z} = \mathbf{E}_\phi(\mathbf{x}_{img})$ into the direction that corresponds to a specific semantic attribute of an image. Given a vector \mathbf{v}_{attr} that encodes a particular semantic aspect in the embedding space and a maximum shift magnitude α , one can construct a sequence of latent codes via manipulation as

$$\left(\mathbf{z}_{man}^{(i)}\right)_{i=1}^k = \left(\mathbf{z} + \alpha \left(\frac{i-1}{k-1}\right) \frac{\|\mathbf{z}_{man}\|}{\|\mathbf{v}_{attr}\|} \mathbf{v}_{attr}\right)_{i=1}^k, \quad (8)$$

where the ratio of norms ensures the strength of manipulation is roughly similar to $\|\mathbf{z}\|$. Analogously to the interpolation case, one can now visualize image effects via plotting tuples $\left(\tilde{\mathbf{E}}_\phi^{-1}(\mathbf{z}_{man}^{(i)}), f_{img}(\mathbf{z}_{man}^{(i)})\right)_{i=1}^k$. While a default choice of $\alpha = 1$ seems to work reasonable well, we find that visually inspecting the manipulated images and choosing α accordingly is recommended in practice. A manipulation vector \mathbf{v}_{attr} can be obtained, for instance, as the normal vector of a hyperplane that separates embeddings of images of two different classes (Preechakul et al., 2022).

Note that attribute manipulation can be seen as a special case of interpolation where one interpolates between \mathbf{z}_{man} and $\mathbf{z}_{man} + \alpha \frac{\|\mathbf{z}_{man}\|}{\|\mathbf{v}_{attr}\|} \mathbf{v}_{attr}$.

3 Experiments with Synthetic Data

To evaluate the capability of our suggested approach in discovering and disentangling the impacts of multiple metric covariates as well as an additional image covariate, we execute an ablation study utilizing synthetic data.

3.1 Data Generation

We generate two synthetic datasets that are generated with several numerical effects as well as an image effect. The first dataset $\mathcal{D}_{\text{squares}}$ ("squares-data") contains images that consist of a white square on grey background such that the white square has half the side length of the total image. The coordinates of the center of the white square are drawn uniformly at random. The image-part of the second synthetic dataset $\mathcal{D}_{\text{colors}}$ ("colors-data") comprises monochromatic images where the red-, green- and blue-values are drawn uniformly at random. Let further Φ_{xval} denote the simple feature-extraction function that maps an image from $\mathcal{D}_{\text{squares}}$ onto the x-coordinate of the center of its white square and Φ_{red} the function that extracts the (average) red value from an image. Note, that we normalize the output of those functions such that Φ_{xval} and Φ_{red} both have the unit-interval $[0, 1]$ as their co-domain. The final image effects are then given by $f_{img} \circ \Phi_{xval}$ for $\mathcal{D}_{\text{squares}}$ and $f_{img} \circ \Phi_{red}$ for $\mathcal{D}_{\text{colors}}$ with $f_{img} \in \{f_{img_1}, f_{img_2}, f_{img_3}\}$ where $f_{img_1}(x) = 2x$, $f_{img_2}(x) = 2x^4$ and $f_{img_3}(x) = \sin(2\pi x)$ (see figure 5).

Besides the image effects, we simulate the effects of the numerical data for $\mathcal{D}_{\text{squares}}$ and $\mathcal{D}_{\text{colors}}$, by using a linear function $f_1(x) = 2x$, a power-function $f_2(x) = x^2$ and a sinusoidal function $f_3(x) = \sin(2\pi x)$. We apply those effects to x-values drawn uniformly at random from the unit interval. Note, that we choose the same form of effects for the numerical- and image-covariate to not allow the model to identify effects over their mere form. We choose f_2 to slightly deviate from f_{img_2} for visualization purposes. To form the response values, we add up all the effects and add zero-centered normally distributed noise $\epsilon \sim \mathcal{N}(0, 0.1)$.

A dataset size of 100,000 samples is used for training the DAE and the NAIM, while additional 10,000 samples are used for testing.

For the visualizations, we display images that correspond to decoded semantic codes for 10 interpolation steps. We then plot the true and the learned effect for those generated images. To have a reference for the generated images, we also display samples that result from a trivial semantic interpolation based on the features extracted by Φ_{xval} and Φ_{red} . To be more precise, for $\mathcal{D}_{\text{squares}}$, we simply linearly interpolate the x-value of the center of the white images and generate the corresponding images. For $\mathcal{D}_{\text{colors}}$ the reference interpolation is obtained by linearly interpolating the red value between the red value of the start-image and the red value of the end-image.

3.2 Results

First, the entire NAIM model is able to almost perfectly predict the correct response-value for the squares data and the colors data since the Mean-Squared-Error of the model is very close to the used noise variance of 0.01 (Table 1). One can also see that including the image covariate, as opposed to using just a NAM, noticeably improves the predictive capabilities even if the image-effect and the numerical effects are very similar or even identical in their structure and magnitude.

3.2.1 NUMERICAL EFFECTS

Regarding the identifiability issue of numerical effects, we also find that the NAIM framework can correctly and accurately identify the effect of several numerical covariates when combined

Squares Data				
$f_{img}(x)$	MSE w/o image	R^2 w/o image	MSE w/ image	R^2 w/ image
$2x$	1.08	0.380	0.0106	0.996
$2x^4$	0.953	0.471	0.0106	0.996
$\sin(2\pi x)$	1.16	0.405	0.0106	0.996
Colors Data				
$f_{img}(x)$	MSE w/o image	R^2 w/o image	MSE w/ image	R^2 w/ image
$2x$	1.08	0.383	0.0106	0.996
$2x^4$	1.03	0.377	0.0106	0.996
$\sin(2\pi x)$	1.21	0.357	0.0122	0.996

Table 1: Overall fit of the NAIM evaluated with a test set of size 10,000 containing image and numerical covariates.

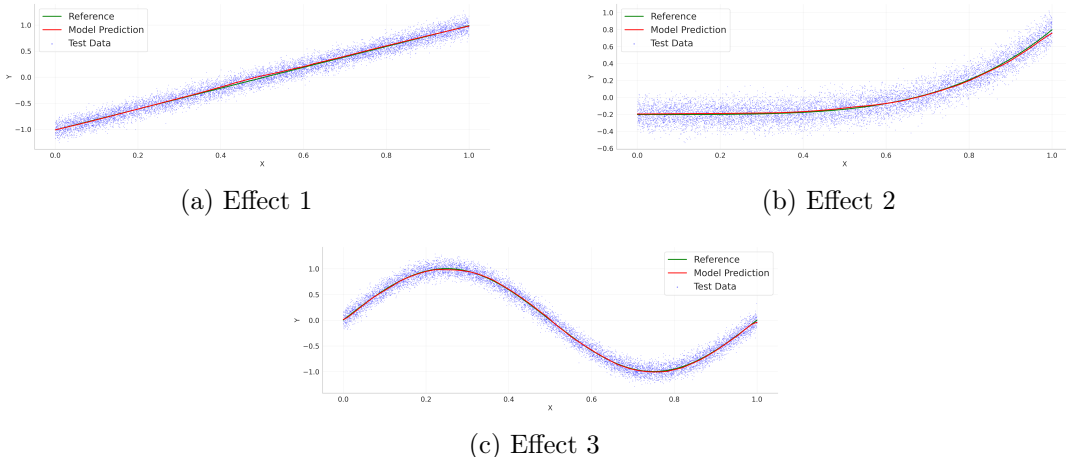


Figure 5: The NAIM models are able to almost perfectly recover the effects of numerical covariates even if an additional image-covariate is present. Effect 1 is a simple linear effect of the form $f_1(x) = 2x$, effect 2 is a power function $f_2(x) = x^2$ and effect three has a sinusoidal form $f_3(x) = \sin(2\pi x)$. This plot shows the discovered numerical effects for the squares-data $\mathcal{D}_{\text{squares}}$ with $f_{img}(x) = 2x^4$ as the image effect of the x-coordinate of the center of the white square.

with an image-effect (Figure 5 and Table 4 in the supplementary material). Note that for plotting purposes, we zero-center the training data and the model’s prediction.

3.2.2 IMAGE EFFECTS

Beyond the numerical covariates, we find that the NAIM model is capable of reliably identifying different image effects among several additive effects. More precisely, we validate the capabilities in recovering the image-effects by choosing 1,000 pairs of images $\mathcal{D}_{\text{pairs}} = \left\{ \left(\mathbf{x}_{img}^{i_1}, \mathbf{x}_{img}^{i_2} \right) \right\}_{i=1}^{1000}$ from the test set of the squares-data $\mathcal{D}_{\text{squares}}$ and the colors data



Figure 6: Visualizing that the NAIM framework can almost perfectly recover a linear effect of the x-coordinate of a white square on grey background in the form $f_{img}(x) = 2x$.

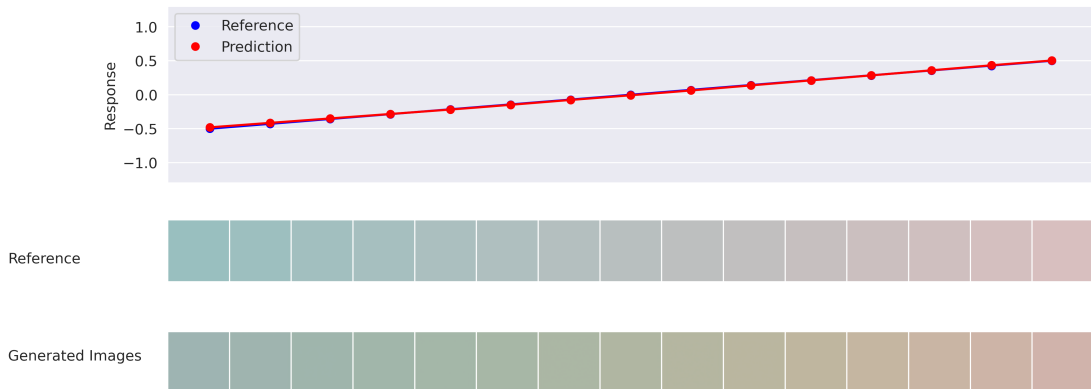


Figure 7: Visualizing that the NAIM framework can almost perfectly recover a linear effect of the red value of monochromatic RGB-image in the form $f_{img}(x) = 2x$.

$\mathcal{D}_{\text{colors}}$, followed by interpolating between the images with 1,000 interpolation steps for each pair. On the one hand, we interpolate with the NAIM between the two elements of the $(\mathbf{x}_{img}^{i_1}, \mathbf{x}_{img}^{i_2})$ tuples, which yields a sequence of semantic subcodes and stochastic subcodes (see section 2.2). On the other hand, we linearly interpolate between the ground-truth features $(\Phi(\mathbf{x}_{img}^{i_1}), \Phi(\mathbf{x}_{img}^{i_2}))$ of the images where $\Phi = \Phi_{xval}$ for $\mathcal{D}_{\text{squares}}$ and $\Phi = \Phi_{red}$ for $\mathcal{D}_{\text{colors}}$. This means we linearly interpolate the position of the white square and the red value of the image, respectively. We then compare the model’s prediction based on the model’s interpolation to the true effect of the linear interpolation of the simple ground-truth features using the mean-squared-error (MSE) and the coefficient of determination (R^2).

Our experimental results show that the NAIM is able to recover and identify the true image-effects reliably by interpolating between individual samples.

Figure 6, 7, 8 and 9 demonstrate that the model can accurately capture and depict image effects.

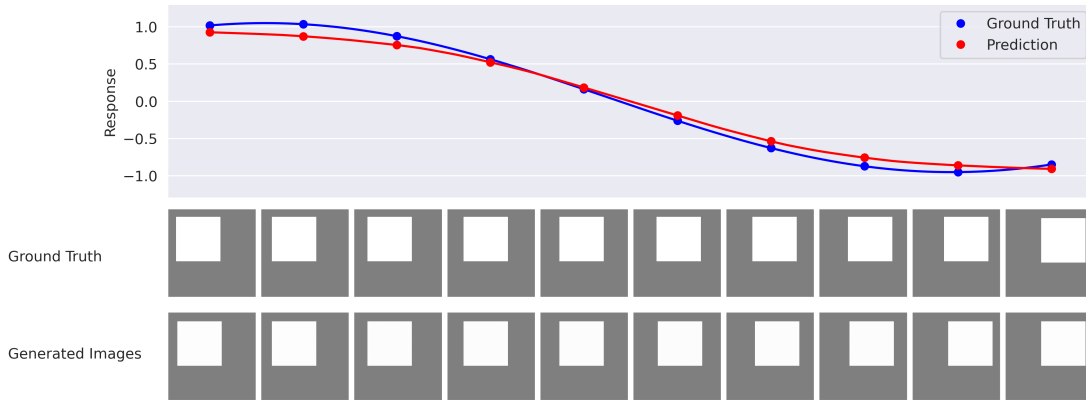


Figure 8: Visualizing that the NAIM-Framework can recover a sinusoidal effect in the form $f_{img}(x) = \sin(2\pi x)$ where x is of the x-coordinate of a white square on grey background.

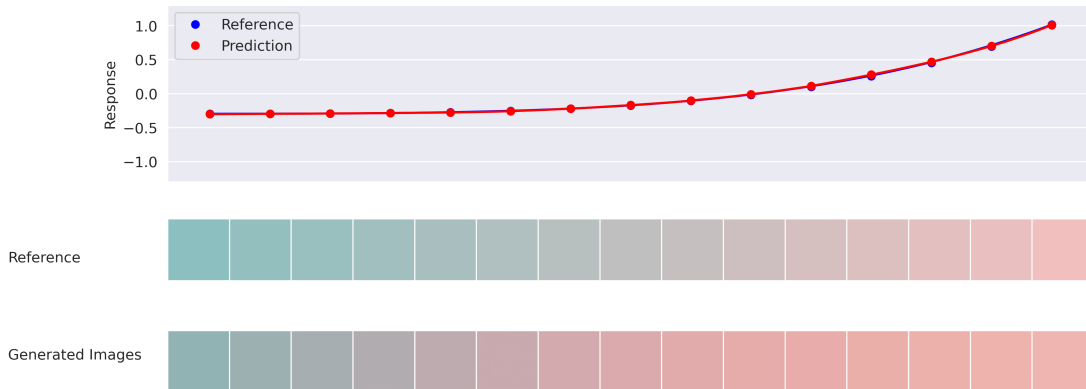


Figure 9: Visualizing that the NAIM-Framework can almost perfectly recover an effect of the form $f_{img}(x) = 2x^4$ where x corresponds to the red value of monochromatic RGB-images.

The interpolation of the latent codes for the square-data corresponds very closely to linear interpolation of the white-square positions (Figure 6 and Figure 8). While the correct linear effect is almost perfectly identified, the decoded images slightly deviate from the reference in case of the colors-data, which is to be expected since semantic interpolation in this case is much less obvious and certainly not unique (Figure 7 and Figure 9).

Note that this ablation study is about an inquiry into assessing how well the model can rediscover a specific data-generating process. We want to stress, that all plots of the effects still allow for a perfect explanation of the model itself, although the model might not be capable of capturing the true data-generating process correctly. Notably, when the model diverges from the real data generation process, its explainability becomes vital in identifying and acknowledging these discrepancies. Thus, the proposed method retains its relevance, even if it does not aim to pinpoint the exact effects.

Squares Data			
Type of image effect	$f_{img}(x)$	MSE	R^2
Linear	$2x$	$1.82 \cdot 10^{-4}$	0.996
Power function	$2x^4$	$3.89 \cdot 10^{-3}$	0.882
Sinusoidal	$\sin(2\pi x)$	$1.33 \cdot 10^{-2}$	0.952

Colors Data			
Type of image effect	$f_{img}(x)$	MSE	R^2
Linear	$2x$	$1.70 \cdot 10^{-4}$	0.968
Power function	$2x^4$	$2.57 \cdot 10^{-4}$	0.933
Sinusoidal	$\sin(2\pi x)$	$1.94 \cdot 10^{-4}$	0.968

Table 2: For benchmarking the capabilities of the NAIM framework in identifying image effect, we compute average MSE and R^2 scores for 1000 randomly selected image pairs from the test set of the squares data and the colors data. This allows to assess how closely the NAIM can recover the true effect of an image covariate. Here, the image effect is computed as the function f_{img} of the x-value of the centroid of a white square for the squares data on grey background and the red value of the image for the colors data.

4 Application

4.1 Data

To assess the effectiveness of the proposed approach for real-world data, we conduct a case study utilizing two Airbnb datasets pertaining to the cities of Cape Town and New York¹. These datasets comprise various types of information, including numerical and categorical features, as well as unstructured data in the form of images. In our analysis, we employ the logarithm of the rental price as the target variable and apply standard normalization to ensure consistency. The available information includes, among further covariates, the number of bedrooms, bathrooms and beds, as well as the average review rating, the total number of reviews and the exact location of the property in the form of longitude and latitude. We preprocess the tabular features by standardizing the numerical covariates and using median imputing for missing values.

Regarding the images, we use the host’s profile pictures that are uploaded by the hosts themselves and that therefore may contain noise. These images typically portray the actual person, with the composition strongly varying depending on the preferences of the users. Therefore, we align the images of the hosts in order to obtain more consistent image sections and head poses, using the alignment procedure employed by Preechakul et al. (2022). Thereby we also discard all images that do not depict human faces and thus we ignore all datapoints where no picture of a human is available. It is also important to note that the variance within the images is still quite substantial and that sometimes an image section showing one person out of a group within the profile picture is selected. By utilizing this rich and diverse dataset,

1. Airbnb is an online platform that allows individuals to rent out their properties to guests for short-term stays. The data can be found under <http://insideAirbnb.com/>.

Table 3: Performance comparison for comparable interpretable additive models. NAM (Agarwal et al., 2021), EBM (Nori et al., 2019) and NodeGAM (Chang et al., 2021) are all fit without the image effect as the architectures of EBM and NodeGAM do not allow to incorporate high dimensional data.

Model	R^2 -score	
	Cape Town	New York
NAM	0.4114	0.4657
NAIM	0.4778	0.5008
EBM	0.4393	0.4783
NodeGAM	0.4241	0.4815

we are able to comprehensively analyze the impact of various image characteristics on rental prices in the Airbnb domain. Through our approach of semantic image interpolation, we seek to uncover the underlying patterns and connections between image semantics and the pricing of Airbnb rentals, providing valuable insights into the factors that drive changes in rental prices based on image attributes. The spatial distribution of the rental offers can be seen in Figure 19 in the supplemental material.

For our analysis, we fit the proposed Neural Additive Image Model (NAIM) including the numerical covariates "room type", "accommodates", "bedrooms", "minimum nights", "number of reviews", "review scores value" and the host image as an image effect. See part A.5 in the supplementary material for more details on the covariates. Compared to equivalently interpretable models that only use those numerical covariates, including the image effect increases the coefficient of determination from $R^2 = 0.411$ to $R^2 = 0.478$ for the Airbnb data from Cape Town and from $R^2 = 0.465$ to $R^2 = 0.508$ for New York (see Table 3). While NodeGAM (Chang et al., 2021) and EBM (Nori et al., 2019) outperform the simple NAM (Agarwal et al., 2021), NAIM outperforms all models for both datasets by also incorporating the image effect.

4.2 Interpretability

First, we demonstrate the global interpretability of the tabular features. Similar to GAMs (Hastie, 2017), NAMs (Agarwal et al., 2021), EBMs (Nori et al., 2019) or NodeGAMs (Chang et al., 2021), the individual feature effects can be visualized without further adjustments. Figures 10a and 10b demonstrate the effects of some of the variables for New York. Global image effects, however, are not as easily visualizable. By shifting the embeddings of all input images $\{\mathbf{E}_\phi(\mathbf{x}_{img}^{(i)})\}_{i=1..n}$ by the same vector into a specified direction and analyzing both, the predictive distribution over all unshifted images, as well as the predictive distribution over the shifted images, we can infer global effects of image characteristics. See section 2.1 for more details on how the vector used to manipulate an attribute is obtained. Figures 10c and 10d show the global effects of the abstract features *attractiveness* and *gender* for Cape Town.

The global effects also become apparent when visualizing them on a sample level. This allows, to not only identify biases on a global level, but to also detect biases for predictions

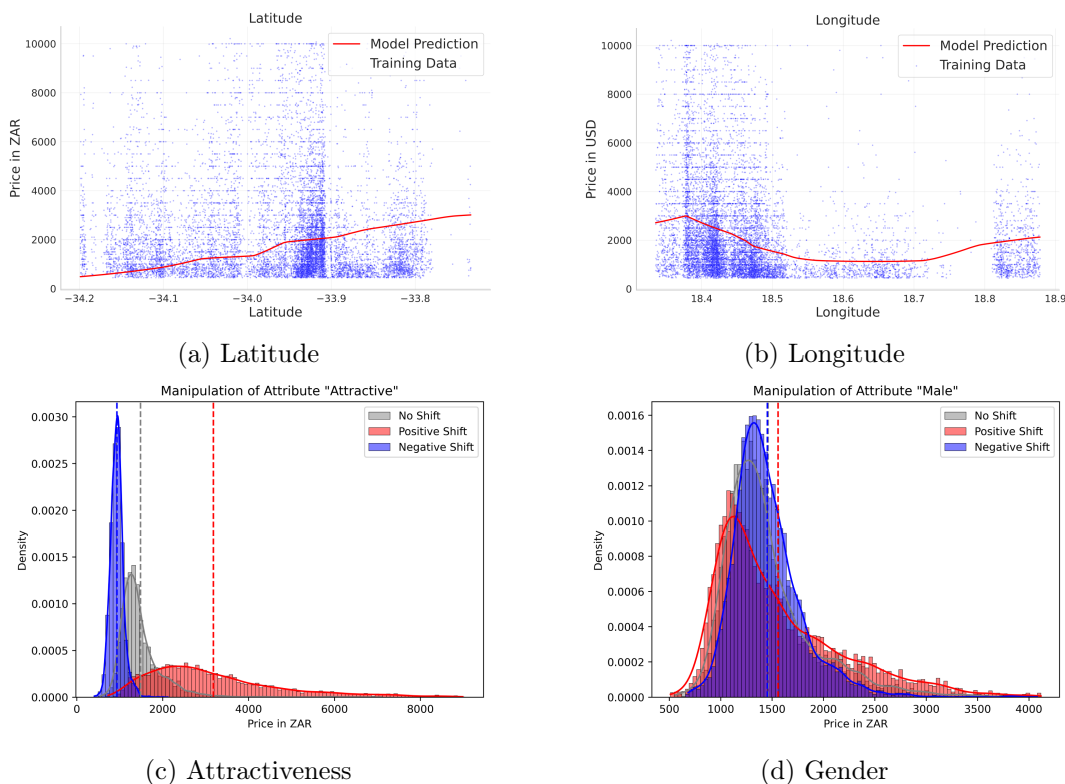


Figure 10: Global interpretation of effects in a Neural Additive Image Model. The effects of numerical covariates can be simply visualized by plotting the corresponding shape functions. The global effect of a certain image features can be analyzed through manipulating all images in the data set analogously and visualizing the shift of the predictive distribution. The grey distribution depicts the original distribution of the predictions for the entire dataset without any manipulation while blue distribution depicts a negative shift and the red distribution depicts a positive shift on the semantic subcode for the chosen feature respectively. We further visualize the means of the distributions with dashed vertical lines.

based on individual examples, and can thus prevent resulting harm in potential real-world decisions. The identified increase of the price for more attractive hosts (Figure 10c) is also identifiable for single hosts. In order not to violate any personal rights we do not depict the real host images for these examples. Instead, we choose examples from the CelebA dataset (Liu et al., 2015). However, the model training as well as the global shifts are all performed on the real host images of the hosts of Airbnb rentals. For the image encoder and the DDIM, we use the weights provided by Preechakul et al. (2022). Figure 4 depicts a positive shift of the host’s image into the direction described as "chubby" in the CelebA dataset. The global effects of this feature can be found in the supplementary material.

Figures 1 and 12 provide a means to visually depict the impact on the expected rental price resulting from an interpolation between the two images shown at the far left and far right. This interpolation effectively captures various attributes, e.g., including skin color and

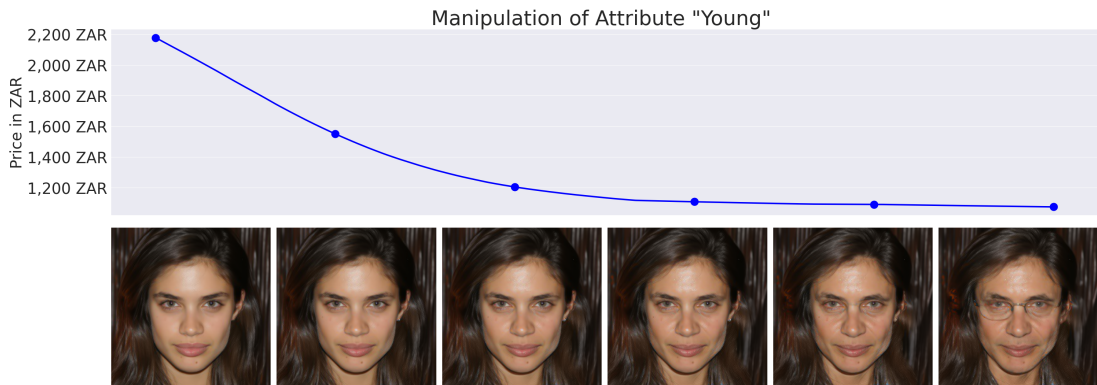


Figure 11: Effect of the feature *age* on the expected rental price. Through (semi) continuous interpolation, an effect trend can be visualized.

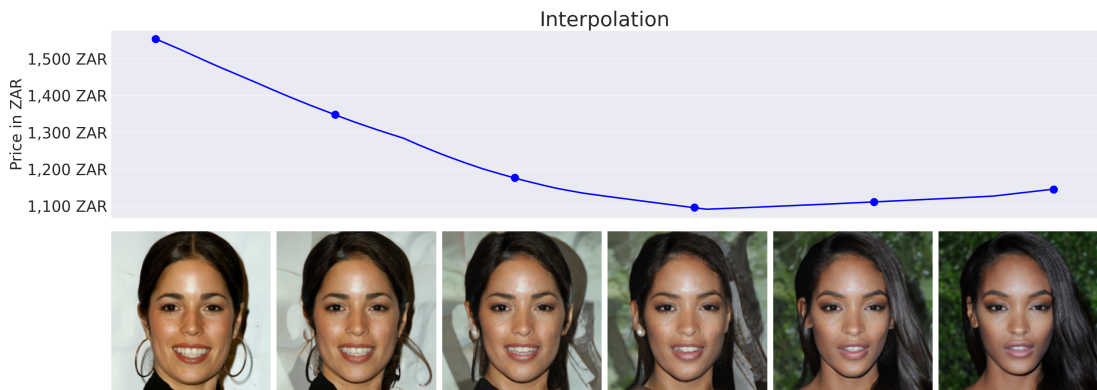


Figure 12: Visualizing the effect of interpolation between two samples on the expected rental price in Cape Town.

hair color and thus also depict attribute interactions. Since no explicit attribute manipulation is needed, interpolation also allows to investigate various features in a very flexible way, depending on the concrete use-case.

5 Broader Impact: On the Importance of Interpretability

Interpretable machine learning models have become increasingly important in real-world applications where transparency and fairness are critical. In particular, additive models have gained popularity due to their ability to provide interpretable and accurate predictions by decomposing the effects of input features into additive components (Jo and Kim, 2022; Chen and Ye, 2022; Moslehi et al., 2022; Siems et al., 2023). However, in the case of image data, the interpretability of additive models has been limited due to the complex and highly nonlinear nature of image features. Especially in the context of fairness and discriminatory effects, image interpretability is a crucial topic in the field of machine learning:

(I) Images can contain highly personal and very sensitive information. In many domains, such as hiring or social media they provide very detailed information on features such as gender, age, body weight or race of a person.

(II) Crucial information is not provided via simple numerical values, but often hidden within partly impenetrable image semantics (e.g. (Pingitore et al., 1994)). The highly complex and somewhat opaque nature of image features makes it very difficult to assess if a given algorithm that relies on image features does actually use morally problematic features for its predictions.

(III) Full intelligibility of image effects allows researchers to interrogate deep learning model behaviors and mitigate system malfunctions.

(IV) As machine learning models become more prevalent in real-world applications, such as job applications, finance or healthcare, the potential for biased decision-making increases, which can be identified with fully intelligible models.

(V) Leveraging complete image intelligibility can be particularly beneficial in the field of medical imaging analysis. The presented approach could uncover valuable insights that may aid in the early detection of diseases and enhance diagnostic quality.

While post-hoc methods, such as LIME (Ribeiro et al., 2016) or Shapely values (Shapley, 1953), are capable to identify important pixel regions, the interpretation of these pixel regions is often not sufficient for generating deep understanding of humanly interpretable image effects and does not allow for a quantification of the image effect. Figure 13 demonstrates, that while relevant pixel areas are identified, they lack any form of easy interpretability. This is especially true for continuous dependent variables, $y \in \mathbb{R}$, since it is not easily interpretable whether the identified pixel regions have positive or negative effects on y . Our presented model thus proposes to rethink the impact of images on numerical features as a form of continuous effect, given that visual attributes are rarely discretely categorizable. For instance, effects that can be extracted from images, such as a person’s hair color, should not be treated as a discrete feature, as there are infinitely many colors between any two hair colors.

By ensuring that machine learning models are fully interpretable and transparent, we can identify, understand and mitigate these biases, promoting fairness and equity in decision-making.

6 Conclusion

In recent years, there has been a growing demand for interpretability in machine learning models, particularly in models that deal with highly complex data. While deep learning approaches have demonstrated high predictive performance, their black-box nature has been a major hurdle for their adoption in fields where interpretability is a key requirement.

To address this challenge, we present a novel approach to account for full interpretability in the context of multi-modal data. We are able to visualize tabular data similarly to Agarwal et al. (2021) and Chang et al. (2021). Additionally, we are able to construct interpretable representations of semantically meaningful image effects. Thereby, we could firstly demonstrate global and a-priori feature interpretability as well as global (see Figure 10) and local (e.g. Figure 11) post-hoc interpretability of image effects. Through interpolation as well as attribute manipulation, the presented approach offers possibilities for image interpretation in a nearly unlimited number of scenarios.

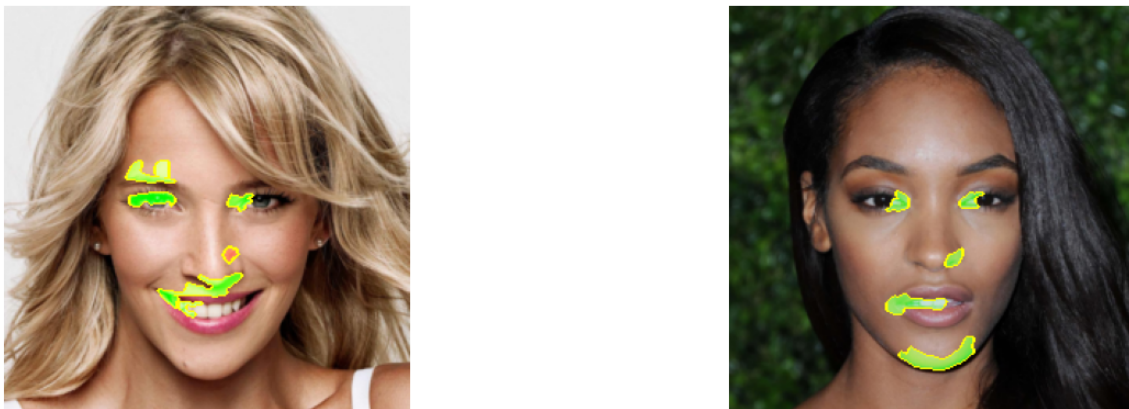


Figure 13: Post-hoc analysis of pixel importance using LIME (Ribeiro et al., 2016) for a regression model predicting expected rental prices based on host images. For data protection reasons, we depict images from the CelebA dataset, instead of using the original images of private persons.

In conclusion, we present an effective approach that addresses the interpretability challenges encountered in modeling multi-modal data. It achieves this by ensuring interpretability at both the feature and image level. This comprehensive interpretability fosters greater trust and deeper comprehension regarding models handling use-cases with multi-modal data, thereby promoting wider acceptance in domains where understanding the model’s inner workings is essential.

7 Limitations and Discussion

The current work offers intelligibility for image effects in multi-modal data problems.

For the NAIM model, we establish identifiability by using feature dropout, as presented by Agarwal et al. (2021) and utilize it to not only drop-out tabular effects, but also the effect of image covariates. However, when assuming that especially high-dimensional image effects can be highly correlated with other features, it might be reasonable to investigate including more recent developments regarding identifiability in the realm of multi-modal data, such as presented in Rügamer et al. (2022); Siems et al. (2024). Those developments might be especially beneficial for our approach when exploring the possibility of including image-image interactions or even interactions between metric features and images.

The presented case study is focused on feature attributes from faces and can thus leverage pre-trained and identified attributes from previous work (Preechakul et al., 2022). The introduced approach, however, is much more general and can be applied to a practically unlimited variety of different images datasets by simply pre-training the autoencoder on the respective data. Furthermore, future work could even investigate the possibility of integrating unstructured covariates other than images, for instance texts.

8 Ethics Statement

Throughout this work we present and showcase a method that can be used to analyze the impact of attributes of Airbnb hosts’ faces on Airbnb prices. Therefore, our method can be used to investigate effects of abstract image attributes such as *attractiveness*, *gender* or *age* that our model might have learned. Thus, our methodology also allows for analyses of biases regarding those features. However, we want to emphasize that appropriately analysing the structure of biases in the used datasets is beyond the scope of this work, in which we aim at introducing and showcasing the method itself. Nevertheless, we want to emphasize that the presented method can indeed have profound societal value in future work, as it can reveal potentially discriminatory effects that can only be identified through interpretable visual analysis.

We train all our models on the true images that are provided by Airbnb directly. However, in this manuscript we demonstrate the visual effects on the CelebA dataset due to privacy concerns.

References

- Rishabh Agarwal, Levi Melnick, Nicholas Frosst, Xuezhou Zhang, Ben Lengerich, Rich Caruana, and Geoffrey E Hinton. Neural additive models: Interpretable machine learning with neural nets. *Advances in Neural Information Processing Systems*, 34:4699–4711, 2021.
- Sebastian Bach, Alexander Binder, Grégoire Montavon, Frederick Klauschen, Klaus-Robert Müller, and Wojciech Samek. On pixel-wise explanations for non-linear classifier decisions by layer-wise relevance propagation. *PloS one*, 10(7):e0130140, 2015.
- Sean Bell and Kavita Bala. Learning visual similarity for product design with convolutional neural networks. *ACM transactions on graphics (TOG)*, 34(4):1–10, 2015.
- Chun-Hao Chang, Rich Caruana, and Anna Goldenberg. Node-gam: Neural generalized additive model for interpretable deep learning. *arXiv preprint arXiv:2106.01613*, 2021.
- Dangxing Chen and Weicheng Ye. Monotonic neural additive models: Pursuing regulated machine learning models for credit scoring. In *Proceedings of the Third ACM International Conference on AI in Finance*, pages 70–78, 2022.
- Padideh Danaee, Reza Ghaeini, and David A Hendrix. A deep learning approach for cancer detection and relevant gene identification. In *Pacific symposium on biocomputing 2017*, pages 219–229. World Scientific, 2017.
- Prafulla Dhariwal and Alexander Nichol. Diffusion models beat gans on image synthesis. *Advances in neural information processing systems*, 34:8780–8794, 2021.
- Abhimanyu Dubey, Filip Radenovic, and Dhruv Mahajan. Scalable interpretability via polynomials. *arXiv preprint arXiv:2205.14108*, 2022.
- James Enouen and Yan Liu. Sparse interaction additive networks via feature interaction detection and sparse selection. *arXiv preprint arXiv:2209.09326*, 2022.

- Feng-Lei Fan, Jinjun Xiong, Mengzhou Li, and Ge Wang. On interpretability of artificial neural networks: A survey. *IEEE Transactions on Radiation and Plasma Medical Sciences*, 5(6):741–760, 2021.
- Trevor J Hastie. Generalized additive models. In *Statistical models in S*, pages 249–307. Routledge, 2017.
- Jonathan Ho, Ajay Jain, and Pieter Abbeel. Denoising diffusion probabilistic models. *Advances in neural information processing systems*, 33:6840–6851, 2020.
- Wonkeun Jo and Dongil Kim. Neural additive models for nowcasting. *arXiv preprint arXiv:2205.10020*, 2022.
- John Jumper, Richard Evans, Alexander Pritzel, Tim Green, Michael Figurnov, Olaf Ronneberger, Kathryn Tunyasuvunakool, Russ Bates, Augustin Žídek, Anna Potapenko, et al. Highly accurate protein structure prediction with alphafold. *Nature*, 596(7873):583–589, 2021.
- Minkyu Kim, Hyun-Soo Choi, and Jinho Kim. Higher-order neural additive models: An interpretable machine learning model with feature interactions. *arXiv preprint arXiv:2209.15409*, 2022.
- Diederik P Kingma and Jimmy Ba. Adam: A method for stochastic optimization. *arXiv preprint arXiv:1412.6980*, 2014.
- Kamran Kowsari, Kiana Jafari Meimandi, Mojtaba Heidarysafa, Sanjana Mendu, Laura Barnes, and Donald Brown. Text classification algorithms: A survey. *Information*, 10(4):150, 2019.
- Ziwei Liu, Ping Luo, Xiaogang Wang, and Xiaoou Tang. Deep learning face attributes in the wild. In *Proceedings of International Conference on Computer Vision (ICCV)*, December 2015.
- Andreas Lugmayr, Martin Danelljan, Andres Romero, Fisher Yu, Radu Timofte, and Luc Van Gool. Repaint: Inpainting using denoising diffusion probabilistic models. In *Proceedings of the IEEE/CVF Conference on Computer Vision and Pattern Recognition*, pages 11461–11471, 2022.
- Pingchuan Ma, Stavros Petridis, and Maja Pantic. Visual speech recognition for multiple languages in the wild. *Nature Machine Intelligence*, pages 1–10, 2022.
- Samad Moslehi, Hossein Mahjub, Maryam Farhadian, Ali Reza Soltanian, and Mojgan Mamani. Interpretable generalized neural additive models for mortality prediction of covid-19 hospitalized patients in hamadan, iran. *BMC Medical Research Methodology*, 22(1):339, 2022.
- Alex Nichol, Prafulla Dhariwal, Aditya Ramesh, Pranav Shyam, Pamela Mishkin, Bob McGrew, Ilya Sutskever, and Mark Chen. Glide: Towards photorealistic image generation and editing with text-guided diffusion models. *arXiv preprint arXiv:2112.10741*, 2021.

- Harsha Nori, Samuel Jenkins, Paul Koch, and Rich Caruana. Interpretml: A unified framework for machine learning interpretability. *arXiv preprint arXiv:1909.09223*, 2019.
- Hyun Oh Song, Yu Xiang, Stefanie Jegelka, and Silvio Savarese. Deep metric learning via lifted structured feature embedding. In *Proceedings of the IEEE conference on computer vision and pattern recognition*, pages 4004–4012, 2016.
- Niall O’Mahony, Sean Campbell, Anderson Carvalho, Suman Harapanahalli, Gustavo Velasco Hernandez, Lenka Krpalkova, Daniel Riordan, and Joseph Walsh. Deep learning vs. traditional computer vision. In *Advances in Computer Vision: Proceedings of the 2019 Computer Vision Conference (CVC), Volume 1 1*, pages 128–144. Springer, 2020.
- Regina Pingitore, Bernard L Dugoni, R Scott Tindale, and Bonnie Spring. Bias against overweight job applicants in a simulated employment interview. *Journal of applied psychology*, 79(6):909, 1994.
- Konpat Preechakul, Nattanat Chatthee, Suttisak Wizadwongsa, and Supasorn Suwajanakorn. Diffusion autoencoders: Toward a meaningful and decodable representation. In *Proceedings of the IEEE/CVF Conference on Computer Vision and Pattern Recognition*, pages 10619–10629, 2022.
- Filip Radenovic, Abhimanyu Dubey, and Dhruv Mahajan. Neural basis models for interpretability. *arXiv preprint arXiv:2205.14120*, 2022.
- Alec Radford, Jong Wook Kim, Tao Xu, Greg Brockman, Christine McLeavey, and Ilya Sutskever. Robust speech recognition via large-scale weak supervision. *arXiv preprint arXiv:2212.04356*, 2022.
- Marco Tulio Ribeiro, Sameer Singh, and Carlos Guestrin. " why should i trust you?" explaining the predictions of any classifier. In *Proceedings of the 22nd ACM SIGKDD international conference on knowledge discovery and data mining*, pages 1135–1144, 2016.
- David Rügamer, Chris Kolb, and Nadja Klein. Semi-structured distributional regression. *The American Statistician*, (just-accepted):1–25, 2022.
- Chitwan Saharia, William Chan, Huiwen Chang, Chris Lee, Jonathan Ho, Tim Salimans, David Fleet, and Mohammad Norouzi. Palette: Image-to-image diffusion models. In *ACM SIGGRAPH 2022 Conference Proceedings*, pages 1–10, 2022.
- L Shapley. Quota solutions op n-person games1. *Edited by Emil Artin and Marston Morse*, page 343, 1953.
- Julien Siems, Maximilian Schambach, Sebastian Schulze, and Johannes S Otterbach. Interpretable reinforcement learning via neural additive models for inventory management. *arXiv preprint arXiv:2303.10382*, 2023.
- Julien Siems, Konstantin Ditschuneit, Winfried Ripken, Alma Lindborg, Maximilian Schambach, Johannes Otterbach, and Martin Genzel. Curve your enthusiasm: Concurvity regularization in differentiable generalized additive models. *Advances in Neural Information Processing Systems*, 36, 2024.

- Jascha Sohl-Dickstein, Eric Weiss, Niru Maheswaranathan, and Surya Ganguli. Deep unsupervised learning using nonequilibrium thermodynamics. In *International conference on machine learning*, pages 2256–2265. PMLR, 2015.
- Jiaming Song, Chenlin Meng, and Stefano Ermon. Denoising diffusion implicit models. *arXiv preprint arXiv:2010.02502*, 2020.
- Nitish Srivastava, Geoffrey Hinton, Alex Krizhevsky, Ilya Sutskever, and Ruslan Salakhutdinov. Dropout: a simple way to prevent neural networks from overfitting. *The journal of machine learning research*, 15(1):1929–1958, 2014.
- Anton Thielmann, René-Marcel Kruse, Thomas Kneib, and Benjamin Säfken. Neural additive models for location scale and shape: A framework for interpretable neural regression beyond the mean. *arXiv preprint arXiv:2301.11862*, 2023.
- Oriol Vinyals, Charles Blundell, Timothy Lillicrap, Koray Kavukcuoglu, and Daan Wierstra. Matching networks for one shot learning. In D. Lee, M. Sugiyama, U. Luxburg, I. Guyon, and R. Garnett, editors, *Advances in Neural Information Processing Systems*, volume 29. Curran Associates, Inc., 2016. URL https://proceedings.neurips.cc/paper_files/paper/2016/file/90e1357833654983612fb05e3ec9148c-Paper.pdf.
- Simon N Wood. *Generalized additive models: an introduction with R*. CRC press, 2017.
- Liangchen Xu and Chonghui Guo. Coxnam: An interpretable deep survival analysis model. *Expert Systems with Applications*, page 120218, 2023.
- Zongsheng Yue, Jianyi Wang, and Chen Change Loy. Resshift: Efficient diffusion model for image super-resolution by residual shifting. *Advances in Neural Information Processing Systems*, 36, 2024.
- Quanshi Zhang, Ying Nian Wu, and Song-Chun Zhu. Interpretable convolutional neural networks. In *Proceedings of the IEEE conference on computer vision and pattern recognition*, pages 8827–8836, 2018.
- Yu Zhang, Peter Tiño, Aleš Leonardis, and Ke Tang. A survey on neural network interpretability. *IEEE Transactions on Emerging Topics in Computational Intelligence*, 5(5): 726–742, 2021.

Appendix A. Supplemental material for Neural Additive Image Models

A.1 Proof of Theorem 1

Proof of Theorem 1 The result follows directly from the definition of total derivatives. In particular, one has

$$h(\lambda \mathbf{z} + (1 - \lambda)\tilde{\mathbf{z}}) = h(\mathbf{z} + (1 - \lambda)(\tilde{\mathbf{z}} - \mathbf{z})) = h(\mathbf{z}) + D_{\mathbf{z}}h((1 - \lambda)(\tilde{\mathbf{z}} - \mathbf{z})) + (1 - \lambda)R_1,$$

where $R_1 = \mathbf{o}(\|\mathbf{z} - \tilde{\mathbf{z}}\|)$. Using that $h(\tilde{\mathbf{z}}) = h(\mathbf{z} + (\tilde{\mathbf{z}} - \mathbf{z})) = h(\mathbf{z}) + D_{\mathbf{z}}h(\tilde{\mathbf{z}} - \mathbf{z}) + R_2$, where $R_2 = \mathbf{o}(\|\mathbf{z} - \tilde{\mathbf{z}}\|)$ and setting $R := R_1 - R_2$, one further obtains

$$\begin{aligned} h(\lambda \mathbf{z} + (1 - \lambda)\tilde{\mathbf{z}}) &= \lambda h(\mathbf{z}) + (1 - \lambda)(h(\mathbf{z}) + D_{\mathbf{z}}h(\tilde{\mathbf{z}} - \mathbf{z})) + (1 - \lambda)R_1 = \\ &= \lambda h(\mathbf{z}) + (1 - \lambda)h(\tilde{\mathbf{z}}) + (1 - \lambda)(R_1 - R_2) = \lambda h(\mathbf{z}) + (1 - \lambda)h(\tilde{\mathbf{z}}) + (1 - \lambda)R, \end{aligned}$$

where clearly also $R = \mathbf{o}(\|\mathbf{z} - \tilde{\mathbf{z}}\|)$.

A.2 Additional results for the experiments with synthetic data

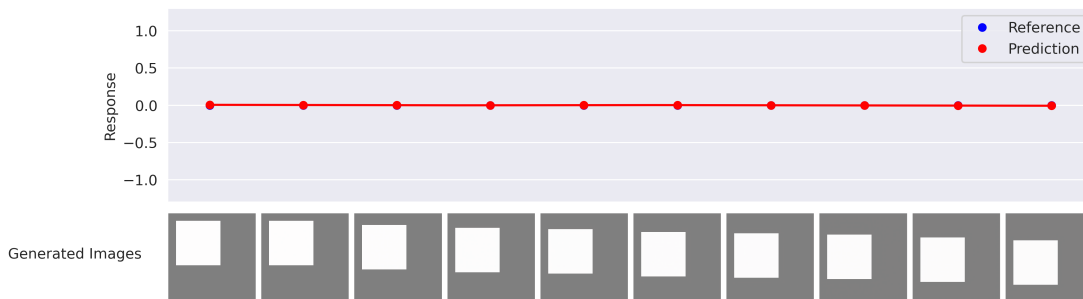


Figure 14: Visualizing that the NAIM-Framework can almost perfectly recover a linear effect of the x-coordinate of a white square on grey background in the form $f_{img}(x) = 2x$. Note that in this case, the effect is expected to be zero since the x-coordiante stays the same.

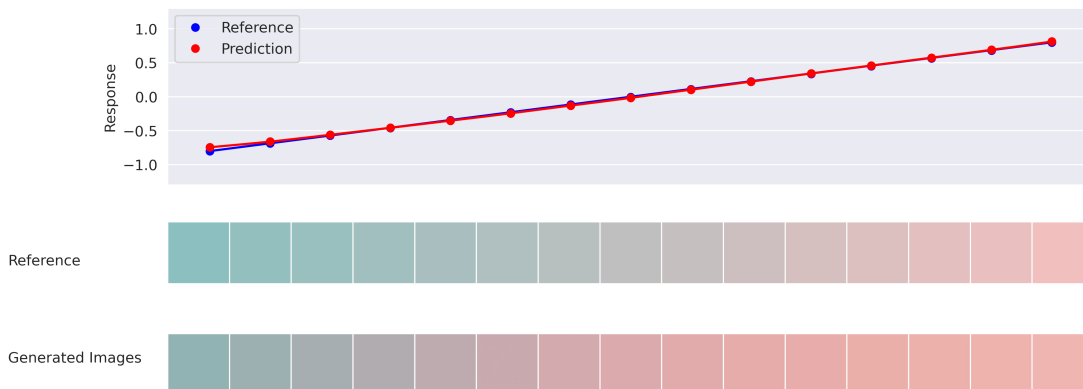


Figure 15: Visualizing that the NAIM-Framework can almost perfectly recover a linear effect of the red value of monochromatic RGB-image in the form $f_{img}(x) = 2x$.



Figure 16: Visualizing that the NAIM-Framework can recover a sinusoidal effect of the red value of monochromatic RGB-image in the form $f_{img}(x) = \sin(2\pi x)$.

Squares Data			
Image effect $f_{img}(x)$	Numerical effect f_i	MSE	R^2
$2x$	$2x$	$5.98 \cdot 10^{-4}$	0.998
	x^2	$4.68 \cdot 10^{-4}$	0.994
	$\sin(2\pi x)$	$9.67 \cdot 10^{-3}$	0.981
$2x^4$	$2x$	$6.85 \cdot 10^{-3}$	0.979
	x^2	$8.15 \cdot 10^{-3}$	0.88
	$\sin(2\pi x)$	$1.28 \cdot 10^{-3}$	0.998
$\sin(2\pi x)$	$2x$	$6.59 \cdot 10^{-3}$	0.980
	x^2	$2.46 \cdot 10^{-3}$	0.966
	$\sin(2\pi x)$	$5.62 \cdot 10^{-4}$	0.999

Colors Data			
Numerical effect f_i	Image effect $f_{img}(x)$	MSE	R^2
$2x$	$2x$	0.0938	0.719
	$2x^4$	$6.59 \cdot 10^{-3}$	0.926
	$\sin(2\pi x)$	0.0396	0.922
x^2	$2x$	0.0465	0.860
	$2x^4$	$3.71 \cdot 10^{-3}$	0.958
	$\sin(2\pi x)$	0.0376	0.925
$\sin(2\pi x)$	$2x$	$5.98 \cdot 10^{-4}$	0.998
	$2x^4$	$4.68 \cdot 10^{-4}$	0.994
	$\sin(2\pi x)$	$9.67 \cdot 10^{-3}$	0.981

Table 4: Assessing the capability of the NAIM to identify effects of numeric covariates when an additional image covariate is present. The MSE and R^2 values are computed between the predicted effect for each f_i and the true value this effect has on a test-set of size 10,000.

A.3 Additional Manipulation Plots

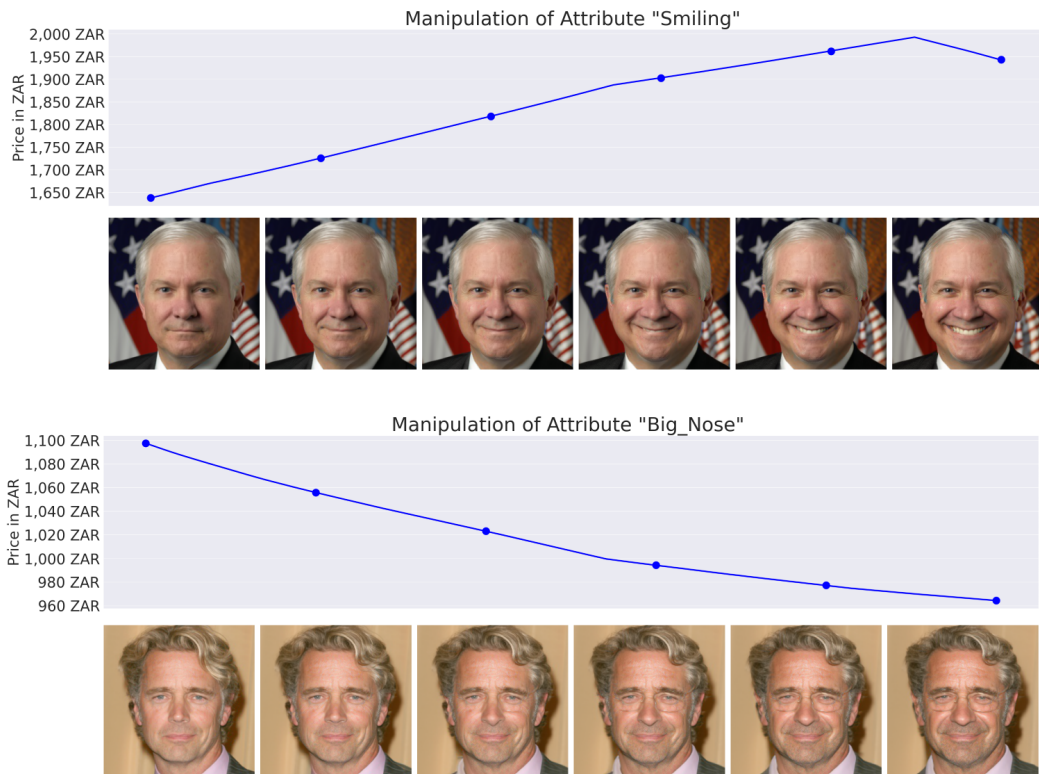


Figure 17: Effect of various facial features on the expected rental price. Through (semi) continuous interpolation, an effect trend can be visualized.

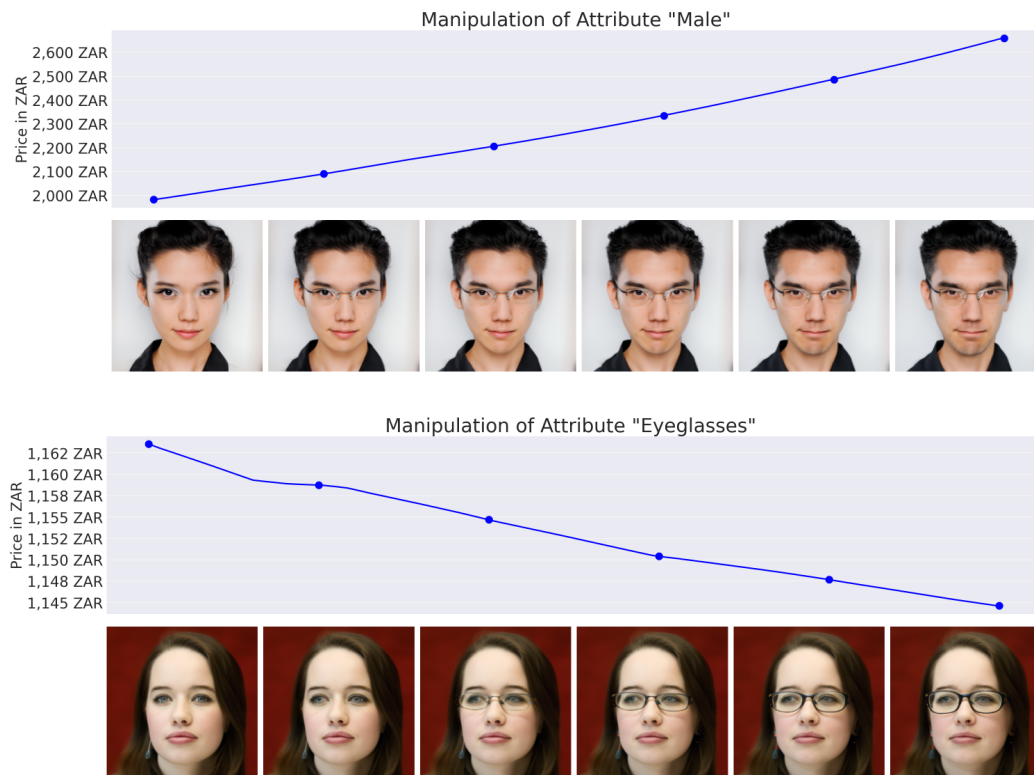


Figure 18: Effect of various facial features on the expected rental price. Through (semi) continuous interpolation, an effect trend can be visualized.

A.4 Descriptive Plots for the Cape Town Dataset

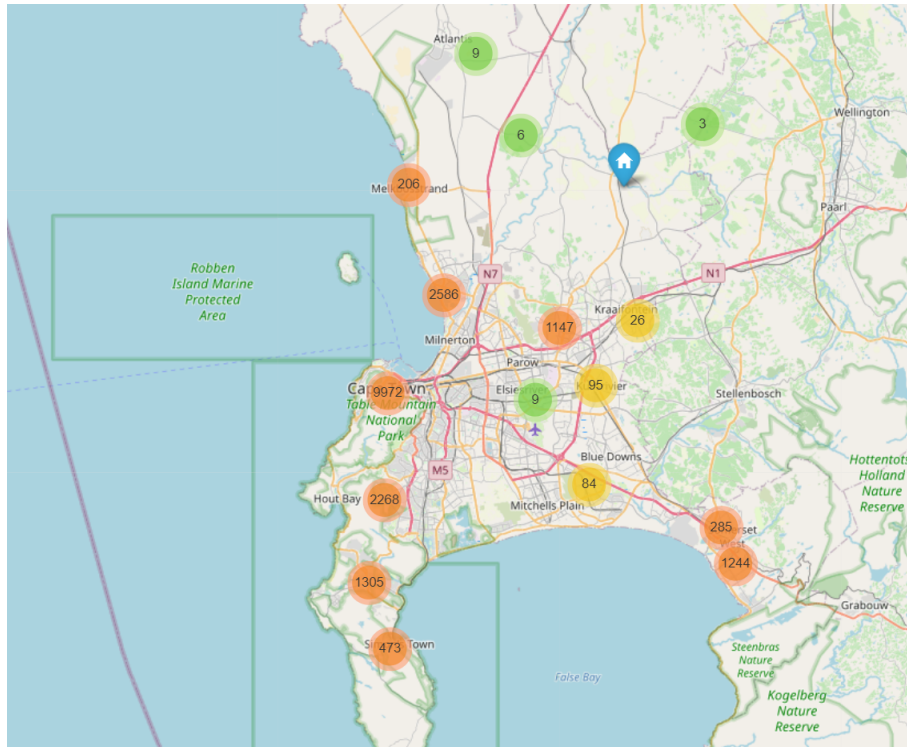
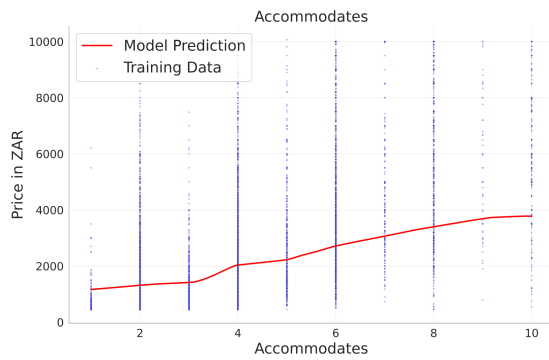


Figure 19: Caption

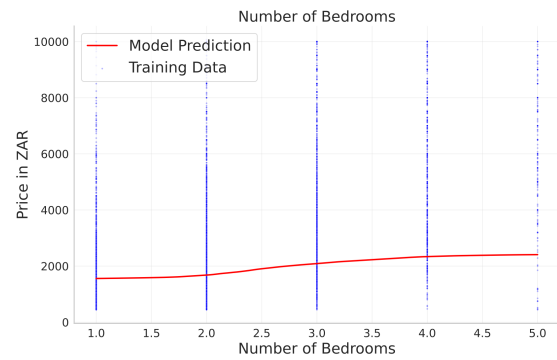
A.5 Explanation of Numerical Covariates for the Airbnb Dataset

Covariate	Data Type	Description
Latitude	Numeric	The latitude of the Airbnb listing's location
Longitude	Numeric	The longitude of the Airbnb listing's location
Room Type	Categorical	The type of room being offered by the host
Accommodates	Numeric	The maximum number of guests allowed
Bedrooms	Numeric	The number of bedrooms available
Minimum Nights	Numeric	The minimum number of nights to book
Number of Reviews	Numeric	The total number of reviews
Review Scores Value	Numeric	The average rating given to the Airbnb listing

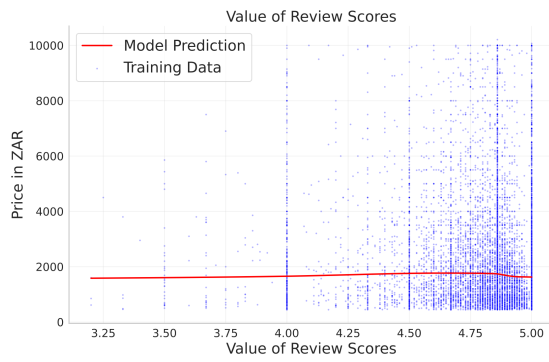
A.6 Effects of Continuous Covariates



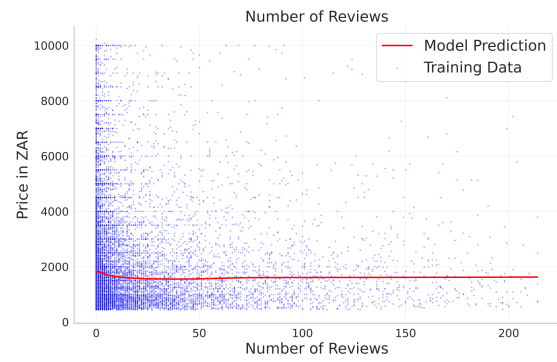
(a) Global effect of the number of accommodated guests on the expected rental price for Cape Town.



(b) Global effect of number of bedrooms on the expected rental price for Cape Town.



(c) Global effect of the average value of review scores on the expected rental price for Cape Town.



(d) Global effect of the number of reviews on the expected rental price for Cape Town.

Figure 20: Global effects of numerical covariates

A.7 Global Image Effects

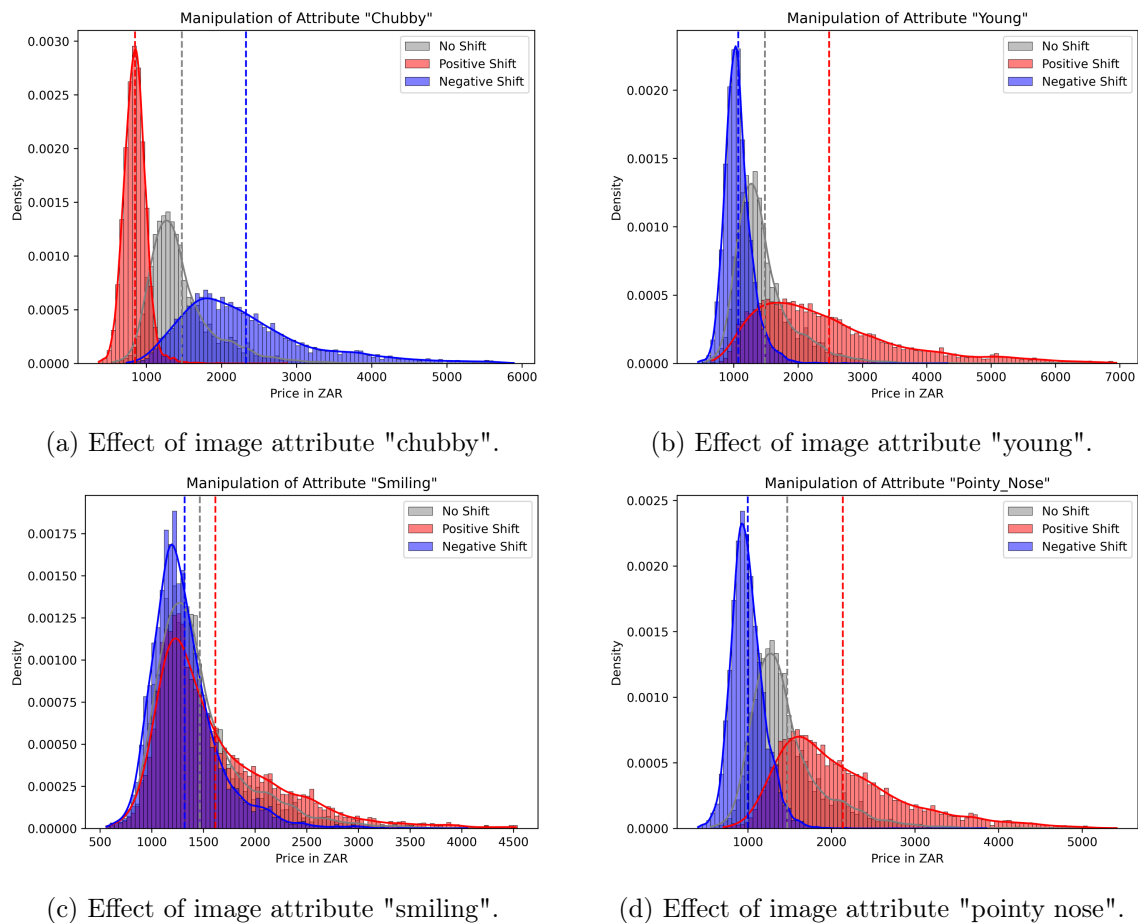


Figure 21: Global effects of images. The global effect of a certain image features can be analyzed through manipulating all images in the data set analogously and visualizing the shift of the predictive distribution. The grey distribution depicts the original predictive distribution without any manipulation while blue distribution depicts a negative shift and the red distribution depicts a positive shift on the semantic subcode for the chosen feature respectively. We further visualize the means of the distributions with dashed vertical lines.

A.8 Hyperparameters

For the synthetic datasets, we utilize the DAE with mostly default hyperparameters (Preechakul et al., 2022). We only deviate from those defaults by setting the batch size to 64 for both datasets and the learning-rate to 10^{-3} for the colors-data. To model the numerical effects and the effect of the embedding of the image effect by the DAE, we use the same architecture. More precisely, we utilize a four-layer MLP with skip-connections and 100 hidden units. We use dropout with a probability of 0.2 (Srivastava et al., 2014) and feature dropout with a probability of 0.5 (Agarwal et al., 2021). We use ReLU activation functions and optimize

the model with a learning rate of 10^{-3} and weight decay parameter 10^{-3} using the Adam optimizer (Kingma and Ba, 2014)

For the AirBnB data, we use the DAE pretrained on Celeb-A (Preechakul et al., 2022). The NAIM uses four-layer-MLPs with 100 hidden units and dropout and feature dropout set to 0.5 in the NAM component and 500 hidden units in a 4-layer MLP for the image-effect component.